INDEX COPERNICUS
INTERNATIONAL

Bio-Algorithms and Med-Systems

WWW.BAMSJOURNAL.COM ISSN: 1896-530X

ORIGINAL ARTICLE

Received: 18.11.2025
Accepted: 03.12.2025
Published: 21.01.2026

CITE THIS ARTICLE AS:
Slotwinski M, Stepien E, Kyziol A, Rawski M, "Cryo-TEM and NTA Characterisation of Hyperglycaemia-Induced Variability in Morphology and Size Distribution of EVs," Bio-Algorithms and Med-Systems vol. 21, special issue New Trends in Nuclear and Medical Physics, pp. 21-28, 2025, DOI: 10.5604/01.3001.0055.5413

AUTHORS' CONTRIBUTION:
A – Conceptualization
B – Data Curation
C – Formal Analysis
D – Funding Acquisition
E – Investigation
F – Methodology
G – Project Administration
H – Resources
I – Software
J – Supervision
K – Validation
L – Visualization
M – Writing – Original Draft
N – Writing – Review & Editing

CORRESPONDING AUTHOR:
MSc Maciej Słotwiński; Department of Experimental Particle Physics and Applications, Cluster of Nuclear Physics Departments, Faculty of Physics, Astronomy and Applied Computer Science, Jagiellonian University, Kraków, Poland; E-mail: maciej.slotwinski@uj.edu.pl

Cryo-TEM and NTA Characterisation of Hyperglycaemia-Induced Variability in Morphology and Size Distribution of EVs

Maciej Słotwiński[1,2BCEFIKLM], Ewa Stępień[2,3ADEFGHJKN], Agnieszka Kyziol[4DEFHN], Michał Rawski[5BEFHIKN]

[1]Department of Experimental Particle Physics and Applications, Cluster of Nuclear Physics Departments, Faculty of Physics, Astronomy and Applied Computer Science, Jagiellonian University, Kraków, Poland
[2]Center for Theranostics, Jagiellonian University, Kraków, Poland
[3]Department of Medical Physics, Faculty of Physics, Astronomy and Applied Computer Science, Jagiellonian University, Kraków, Poland
[4]Coordination and Bioinorganic Physicochemistry Group, Faculty of Chemistry, Jagiellonian University, Kraków, Poland
[5]SOLARIS National Synchrotron Radiation Centre, Jagiellonian University, Kraków, Poland

ABSTRACT

Introduction: Extracellular vesicles (EVs) are membrane-bound structures that play a crucial role in intercellular communication and molecular transport. Due to their biological functions, EVs hold great potential as a novel diagnostic tool or as the targeted drug carriers in anticancer therapies. Elevated glucose concentrations affect cellular metabolism, thereby modifying the composition of the EVs and their lipid bilayer. This, in turn, can influence EVs' properties and morphology, which is important in their function.
Hypothesis: Hyperglycaemic conditions, by altering the composition and metabolism of EVs, influence their size distribution and physicochemical properties.
Objective: Visualisation and size distribution comparison of EVs isolated from normoglycaemic (NG) and hyperglycaemic (HG) conditions.
Methods: Two complementary methods based on different physical principles were applied and compared in terms of their applicability: nanoparticle tracking analysis (NTA) and cryo--transmission electron microscopy (Cryo-TEM). In this study, 1.1B4 cells were cultured in normo- (NG, 5 mM glucose) and hyperglycaemic (HG, 25 mM glucose) conditions.
Results: The mean hydrodynamic EV size under hyperglycaemic conditions (236 ± 28 nm) was slightly higher than the control (209 ± 43 nm; Paired Sample Wilcoxon Signed Test, $p = 0.05$). Physical EV sizes (Cryo-TEM), as well as mode hydrodynamic sizes (NTA) were consistent and not affected by glucose concentration. In contrast to NTA, Cryo-TEM is a more precise technique for real-size distribution analysis, whereas NTA provides a rapid and cost-effective assessment of hydrodynamic radii. The theoretical level of detection of NTA for EVs was close to what was observed in results.
Conclusions: Hyperglycaemic conditions slightly influenced only the mean hydrodynamic radius of EVs, indicating effects on EV corona size and the biogenesis of large EVs (lEVs).

KEYWORDS

exosomes, extracellular vesicles, glucose, pancreatic β-cells, Cryo-TEM, nanoparticle tracking analysis

BRIEF DESCRIPTION OF THE WORK

This study investigates how hyperglycaemia alters the size distribution and morphology of extracellular vesicles secreted by human pancreatic β-cells (1.1B4) using Cryo-TEM and NTA techniques. Understanding glucose-induced EV changes may support the development of EV-based diagnostics and drug delivery strategies.

LIST OF ABBREVIATIONS

DM – Diabetes Mellitus
EVs – Extracellular Vesicles
HG – hyperglycaemic conditions
lEVs – large Extracellular Vesicles
lncRNAs – long noncoding RNAs
LOD – Level Of Detection
MVs – microvesicles
NG – normoglycaemic conditions
NTA – Nanoparticle Tracking Analysis
PBS – Phosphate-Buffered Saline
sEVs – small Extracellular Vesicles

INTRODUCTION

Extracellular vesicles (EVs) are nanosized, lipid bilayer-bound vesicles secreted into body fluids. The EVs possess an ability to transport different cellular material or genetic information [1]. In addition, as described by Yáñez-Mó et al. (2015), almost all cells produce these types of vesicles, and they can be found in all body fluids [2]. Moreover, in their lipid bilayer, specific proteins can be found, facilitating the recognition of distinct vesicles. Furthermore, because of their native function in the body, they play a crucial role in maintaining homeostasis [3]. Thus, there is a major potential for their use not only as drug carriers but also as biomarkers or immune system modulators.

The EVs are divided into more than 20 different subpopulations. Among them there are 8 vesiculated EVs, which include small extracellular vesicles (sEVs) and large extracellular vesicles (lEVs) [4]. The smaller ones (sEVs) are also commonly known as exosomes. For them, generally a 30- to 150-nm size range is used [5]. However, their definite categorisation is still in the process, and different size ranges are utilised [4]. Above the diameter of 100 nm up to 1000 nm, the large extracellular vesicles (lEVs) are present. Other names used are microvesicles (MVs) or ectosomes, although size is not the most important factor in their classification. The EVs differ in the mechanism of their biogenesis and their molecular cargo (proteins, sugars, DNA, mRNAs, microRNAs [miRNAs], long noncoding RNAs [lncRNAs] and lipids). Another important feature of EVs is the lipid bilayer corona. It consists in part of the transmembrane proteins, but the majority is made up of glycans (carbohydrates linked with surface proteins) [1].

Normal concentration of glucose in blood ranges between 3.9 mM and 5.6 mM when fasting for 8 h, or below 7.8 mM, 2 h postprandial. When it reaches more than 6.9 mM or 10 mM, subsequently, hyperglycaemic conditions are assumed for fasting and postprandial, and a patient is called diabetic [6]. It can be caused by a large number of factors, which often in the early stages can be downplayed. When left unrecognised this can lead to serious damage in the body and cause significant complications. There are many causes that lead to the development of chronic hyperglycaemia, starting from diabetes mellitus (DM), strokes [7], myocardial infarctions [8] or major surgeries [9], and ending at excess secretion of hormones, such as cortisol, catecholamines, growth hormones or glucagon [10]. Due to the occurrence of hyperglycaemia in the blood, many of its characteristics are altered. Since blood is responsible for many pathways, altering its parameters by high concentration of glucose can lead to a multitude of pathogenic conditions and modifications in the composition of the EVs [11] and their lipid bilayer [12].

METHODS

Cell-line authenticity

Cells from the 1.1B4 cell line were used (Sigma-Aldrich; 10012801). At the moment of publication, Sigma-Aldrich has discontinued sales of this cell line. To confirm the origin and purity of the line, genetic authentication (Supplementary Fig. 1.) was commissioned to Eurofins Genomics Europe Applied Genomics GmbH (Ebersberg, Germany). The analysis result indicates the 1.4E7 line. After manual verification, the markers identified in the sample mostly match the pattern for the 1.1B4 cell line. The only difference was that, in some cases, double homozygous signals (e.g. 11,11) were observed in the acquired cell line, whereas the pattern in the database displays was a single 11.

Cell culture

Two parallel cell cultures were performed in distinct conditions: Normoglycaemic (NG – concentration of D-(+)-glucose = 5 mM) and Hyperglycaemic (HG – concentration of D-(+)-glucose = 25 mM). Other cell culture conditions were as follows: 37°C, 5% CO2, RPMI1640 growth medium, 10% FBS, 2 mM L-glutamine, 100 I.U./mL of penicillin and 100 µg/mL of streptomycin. For the isolation of EVs the following passages were used: NG = 33; HG = 43. Cell morphology comparison is depicted in Fig. 1.

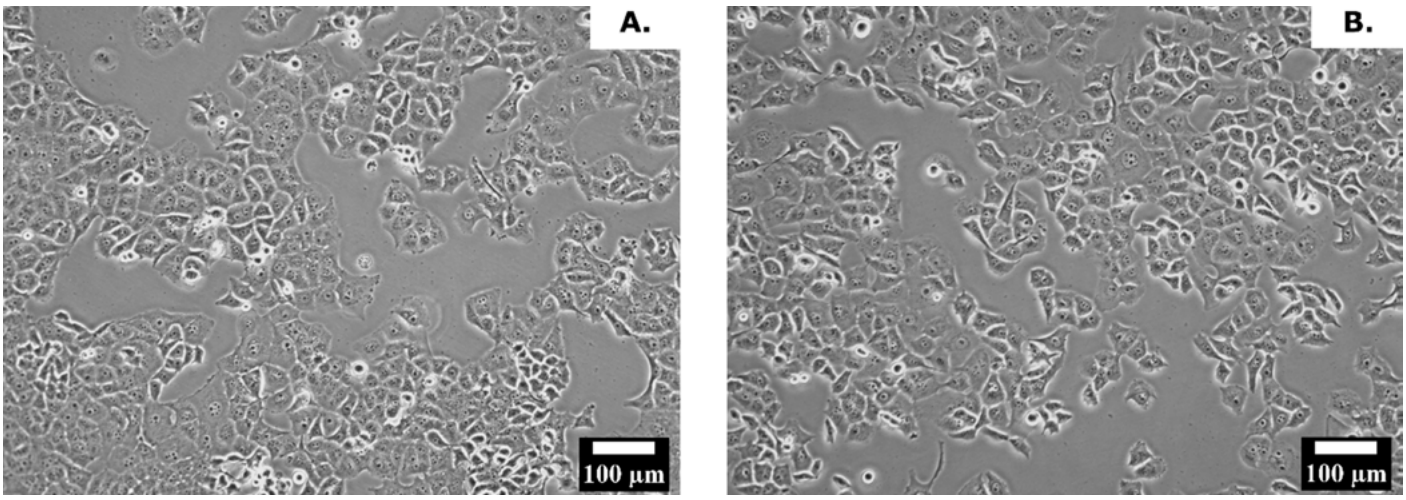

Fig. 1. Micrographs of 1.1B4 cells: (A) Normoglycaemic conditions; (B) Hyperglycaemic conditions. There were no morphological changes in the cells under applied conditions.

Tab. I. Differential centrifugation protocol, including the membrane filtration step (rt – room temperature).

ORDER OF STEPS IN ISOLATION	ACCELERATION [g]	TIME [min]	TEMPERATURE
1.	500	10	rt
2.	3,000	25	rt
3.	7,000	30	rt
4.	Membrane filtration		rt
5.	18,000	20	4°C
6.	150,000	90	4°C

Sample preparation

After the cells reached a confluence of around 80–90%, a medium without FBS was added. Twenty-four hours later, isolation was performed with the use of a differential centrifugation. Tab. I. contains subsequent centrifugations with the step of the membrane filtration. During the process of differential centrifugation, each time after centrifugation had ended the supernatant was transferred into a new falcon tube. Sterility was not maintained. To inhibit the growth of the bacteria and other microorganisms, a solution of sodium azide was added (a concentration of 0,02% in the sample was used).

The setup for membrane filtration was made of a dialysis tubing (Biotech CE Dialysis Tubing 1000KD; Repligen) attached to a funnel, fitted airtight through a vacuum bottle screwcap. The lower end of the membrane was folded three times, closed with parafilm and clipped with a dialysis tubing closure. The setup was then connected to a vacuum pump. The validity of a membrane was assessed by filling the funnel with deionised water and checking the dripping rate (optimal dripping rate ~1 drop/s). No leaks were visible. After nearly all the media had filtered through, the funnel was filled again with deionised water and topped up until all residual colour from the growth medium disappeared. After washing the inside of the membrane twice with deionised water, approximately 5–6 mL of the concentrated EV suspension remained.

NTA

Nanoparticle tracking analysis was performed using a NanoSight NS300 instrument equipped with a 532-nm green laser (Malvern Panalytical). Samples were diluted 100-fold in a phosphate--buffered saline (PBS) to obtain a particle concentration of approximately 20–100 particles per field of view (Fig. 2.). All solvents were prefiltered through a 0.45 µm filter. A blank measurement was recorded before sample loading. Each sample was measured in at least nine technical replicates (60 sec each). The resulting data was averaged for analysis. The maximum camera shutter speed was used (1500), resulting in videos of 25 frames per second. Camera gain and histogram ranges were adjusted accordingly to increase the signal-to-noise ratio. The detection threshold was set manually for each measurement. Depending on the noise intensity, the detection threshold varied from 3 to 5. For NG samples, 29116 EVs were detected (4 biological replicates, a total of 56 technical repetitions), and for HG samples 31662 EVs (4 biological replicates, a total of 52 technical repetitions). Fig. 2. presents representative NTA video frames.

Determination of the level of detection (LOD) for the NTA measurement of EVs

To determine if LOD may impact NTA EV size distribution, an

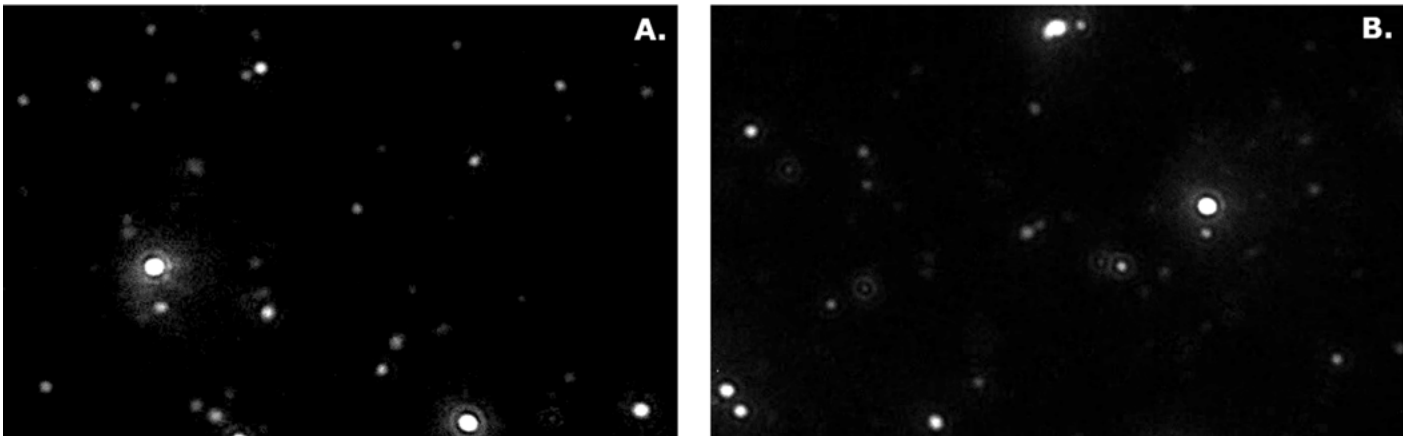

Fig. 2. Representative images from the NTA videos recorded for size distribution analysis: (A) NG sample; (B) HG sample.

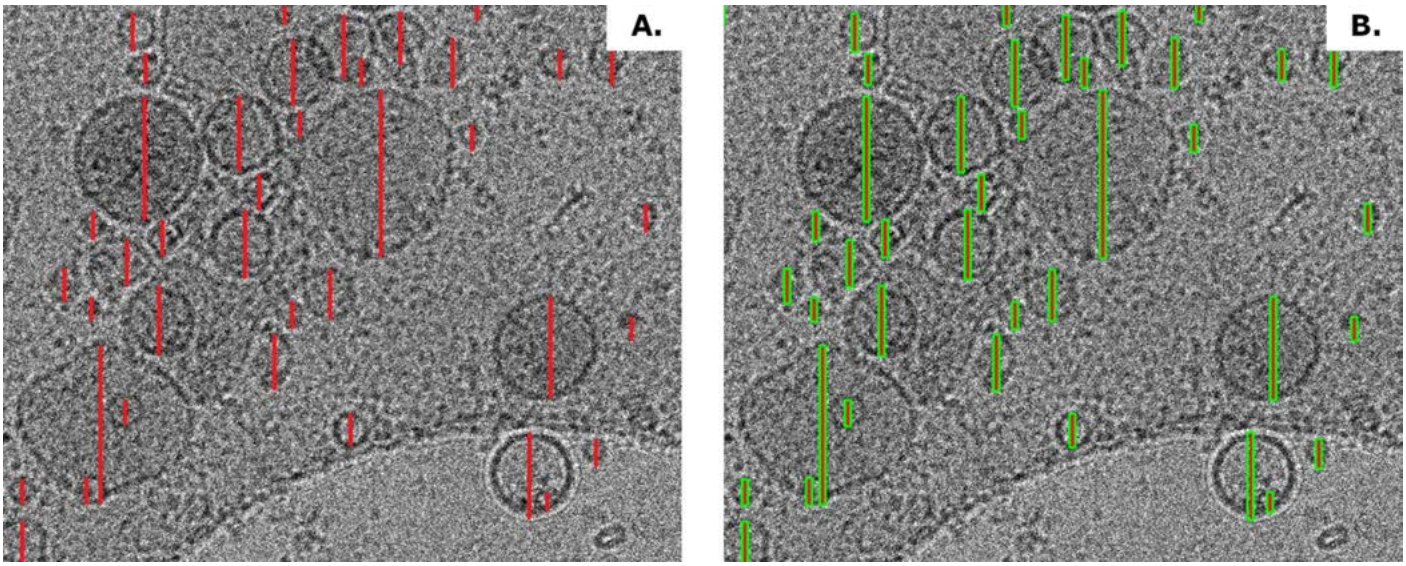

Fig. 3. Detection of EV radii with the usage of a custom Python script on the Cryo-TEM images: (A) Hand-marking of the EVs with the red lines; (B) The green overlay confirming a correct detection of marked lines.

inquiry into its boundary should be made. For the NanoSight NS300 apparatus a manufacturer gives a detection range of 10–1000 nm [13]. The LOD was specified for nanoparticles with high refractive indices (Ri), such as gold or silver, with their Ri ranging from 2 to 4 [14]. The Ri of EVs varies depending on their size, origin and the laser used. Values ranging from 1.36 for sEVs to 1.41 for lEVs were specified, resulting in a theoretical LOD between 30–50 nm [15, 16]. Physical LOD was determined by van der Pol et al. (2014) at 70 to 90 nm [17]. During measurements, EVs were often detected below 100 nm, at around 72 ± 16 nm. In conclusion, the LOD should not influence the analysis on the acquired NTA histograms.

Cryo-TEM

Measurements were conducted at the National Synchrotron Research Centre SOLARIS at Jagiellonian University. As a sample carrier, QUANTIFOIL R2/1 copper grids, mesh 200, were used. The grids were cleaned and functionalised in air plasma by glow discharging. Afterward they were placed inside the Vitribot mkIV (ThermoFisher Scientific). Next, a 5 µL sample was put onto the hydrophilic side of the grid and immediately plunged into the liquid ethane. Following vitrification, the samples were stored in grid boxes in a LN2 storage tank. Before imaging, the grids were clipped with copper rings and kept in liquid nitrogen throughout the transfer procedure.

Cryo-TEM image analysis

To obtain the size distribution from Cryo-TEM images, a custom Python script was developed [17]. The script detected vesicle diameters based on hand-marked lines, so fundamentally the EVs were measured manually (Fig. 3A). A verification function overlaid green perimeters on detected lines, enabling the identification of undetected or incorrectly measured features (Fig. 3B). Accuracy was validated against a representative image. Out of 1,791 measurements, 5 lines (0.28%) were not detected and 4 (0.22%) were misidentified; these were manually corrected.

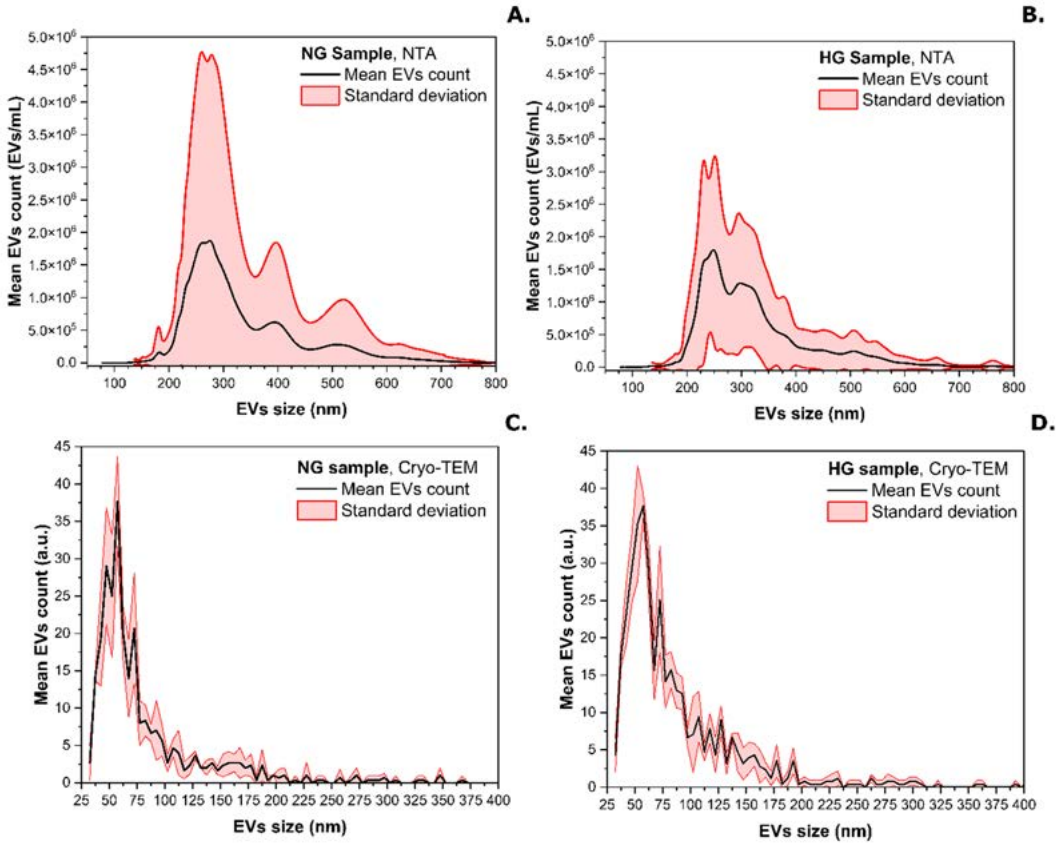

Fig. 4. Histograms with standard deviations plotted for: (A) NTA, NG samples; (B) NTA, HG samples; (C) Cryo-TEM, NG samples; (D) Cryo-TEM, HG samples.

For NG samples, 828 EVs were detected (3 images, 1 biological replicate), and for HG samples 963 EVs (4 images, 1 biological replicate). Measurements were highly precise, with an average mean value obtained from 7 Cryo-TEM images of 54 ± 3 nm. For analysis, EVs sizes were grouped by 5 nm to smooth the histograms. The low number of biological replicates was caused by limited access to the Cryo-TEM apparatus. Mean Cryo-TEM histograms were normalised to the maximum count of EVs from NTA.

RESULTS

Analysed Cryo-TEM images are included in the Supplementary Fig. 2. Histograms from all the samples were averaged, and standard deviations were calculated (Fig. 4.).
To minimise the standard deviations, the EV counts were normalised to the cell counts from which the EVs were isolated, although this process did not bring any improvements to the shape or standard deviations of histograms. Large standard deviations are caused by the specificity of the appropriate method and the heterogeneity of the samples of biological origin. Mean histograms for respective biological replicates also possess high standard deviations (Supplementary Fig. 3.).

Calculated standard deviations for the Cryo-TEM method were significantly lower than those for NTA, even though the number of samples, as well as the detected EVs, was much smaller. The roughness of the Cryo-TEM histograms was caused by a small number of replicates. The mean histograms were normalised to the maximum count of EVs for both NTA and Cryo-TEM data (Fig. 5.).

As presented in Fig. 6., for both mean and mode values, a large increase in diameter was observed for the NTA method. The shift between presented histograms was 121 ± 37 nm on average, and it is statistically significant (Mann-Whitney U Test, $p = 0.0001$). The reason for that lies in different measurement principles. The NTA provides us with the hydrodynamic radius of the vesicles suspended within the medium. It is also affected by the EV corona, which is usually not visible in Cryo-TEM images.

To compare the two cell-culture conditions, mean and mode values for each sample (NG and HG) were averaged. The mean hydrodynamic size of the EVs isolated from the 1.1B4 cell line (Fig. 6A.) was slightly higher for hyperglycaemic conditions (236 ± 28 nm) than normoglycaemic ones (209 ± 43 nm). The difference between mean values (for respective technical repetitions) was found to be statistically significant (Paired Sample Wilcoxon Signed Test, $p = 0.05$). Physical sizes stayed the same, averaging 86 ± 7 nm for both conditions combined.

The mode values (Fig. 6B.) were consistent within each method, with combined NG and HG conditions averaging 54 ± 3 nm for

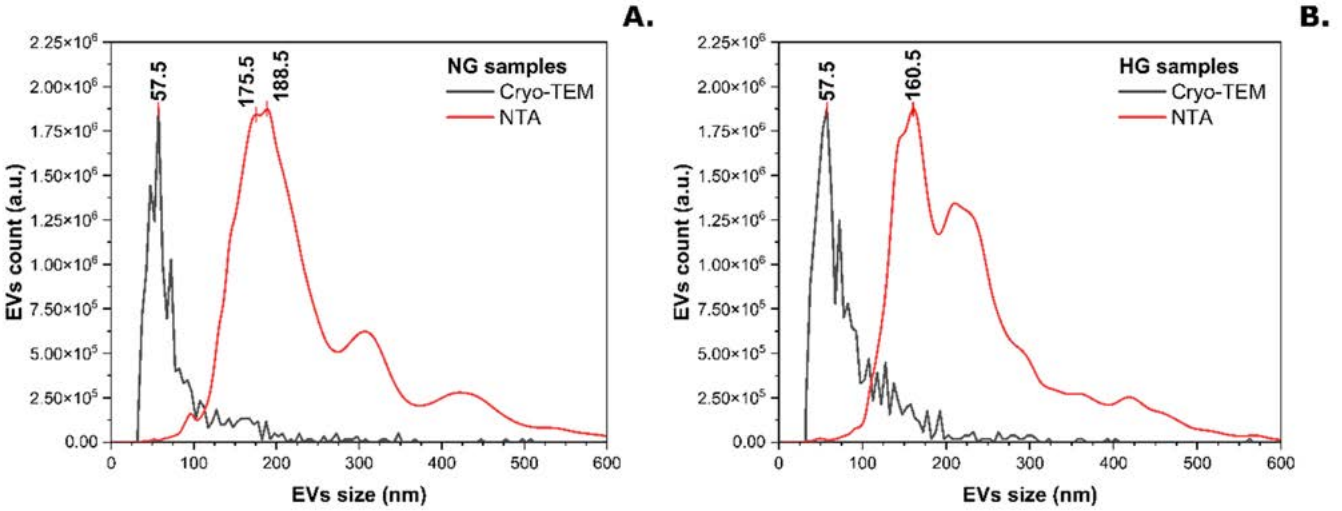

Fig. 5. Imposed histograms of NTA and Cryo-TEM data (normalised to the maximum count of EVs): (A) NG samples; (B) HG samples.

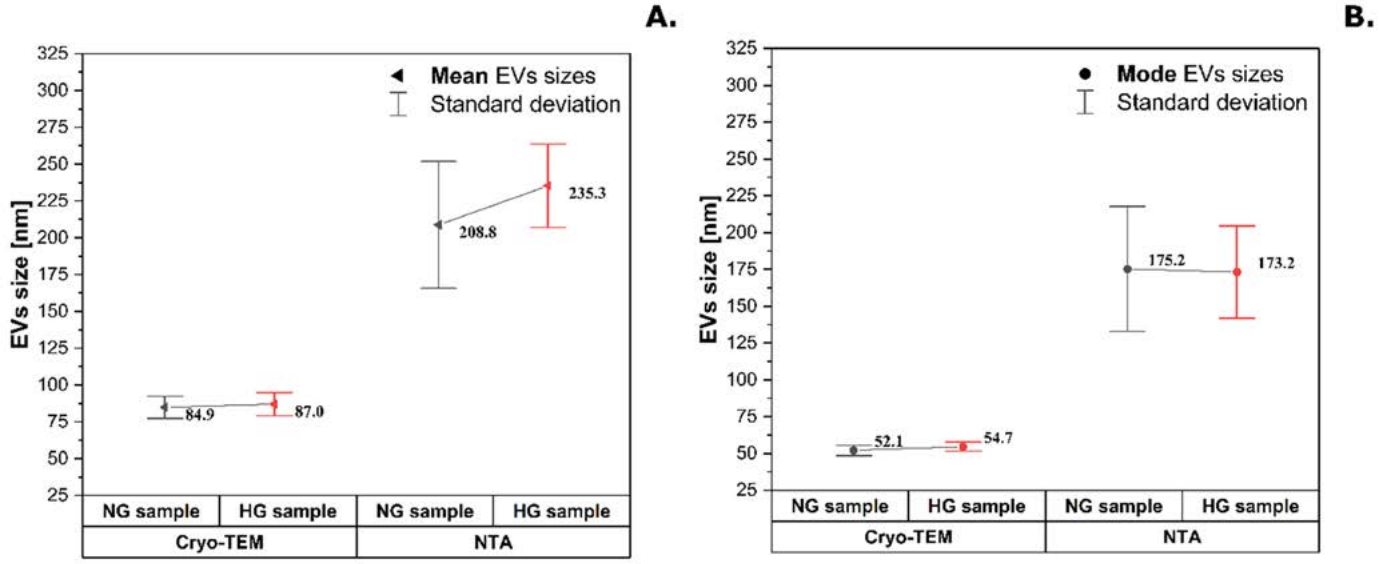

Fig. 6. Comparison of average values for NTA and Cyro-TEM measurements: (A) Mean sizes; (B) Mode sizes.

Cryo-TEM and 174 ± 37 nm for NTA. The discrepancies between calculated mode values and those presented in Fig. 5. are not significant and fall within the calculated standard deviations.

DISCUSSION

A higher mean value of the hydrodynamic radius for the HG conditions (NTA) was found to be statistically significant (Paired Sample Wilcoxon Signed Test, $p = 0.05$). Together with a lack of change in the Cryo-TEM data, it can be concluded that hyperglycaemic conditions influence only the hydrodynamic size of the vesicles. The mode hydrodynamic size being almost the same (174 ± 37 nm for NG and HG combined) suggests that only the larger EVs are affected. This could mean that in hyperglycaemia the mechanism for lEVs production is altered (due to outward budding of the cell membrane), while the one for sEVs stays the same (due to inward budding of the endosomal membrane). Hyperglycaemic conditions influence protein and lipid composition of EVs [11, 12, 18], yet no research was previously conducted to analyse their influence on the size of the corona. To verify this occurrence further research would be needed, including visualisation of the EV corona, for example, with negative contrast TEM [19].

There is a clear difference between the histograms obtained from Cryo-TEM and NTA (Fig. 5A., B.), which arises from their distinct measurement principles. Cryo-TEM produces “images” of EVs by exposing them to an electron beam, whereas NTA

illuminates the particles with a laser, detects the scattered light and tracks their Brownian motion. Because of that, from the NTA result we determine a hydrodynamic radius which is far larger than the physical one and depends on the structure of the EV corona and solvation shell size. It has been reported that the solvation shell for EVs can vary from 10 to 20 nm [20]. On the other hand, sizes of the EV corona are said to be around 5–15 nm [19, 20], so together with the solvation shell it would amount to around 35 nm, not explaining the 120-nm shift observed on average; however, the corona sizes may vary depending on the cell line used. Measurements often revealed EVs smaller than 100 nm, with a diameter around 72 ± 16 nm, so with the estimated LOD of 70–90 nm, the size distribution should not be affected by it, although for definitive conclusions independent inquiry into the limit of detection for the used apparatus should be performed [21].

Differences in mean and mode values are clearly seen in both methods. The higher mean values are caused by the heterogeneity of the EV samples. As observed in Fig. 5., there is a high count of vesicles above the mode values. On top of that, size distributions measured by Cryo-TEM and NTA have similar shapes. This suggests that both methods are complementary and, with appropriate assumptions, can be considered valid independently for size distribution analysis [22, 23]. Furthermore, histogram shapes closely resemble the theoretical model for EV's isolation, developed by M. Durak-Kozica et al. (2022), in which the subsequent steps in the differential centrifugation protocol were modelled based on EV density [24]. The small standard deviations of Cryo-TEM histograms indicate that the procedure of hand-marking EVs did not compromise the precision of the applied method.

It is noteworthy that Cryo-TEM histograms can be used for validation of the isolation protocol as well. In the size distributions mostly sEVs are present (vesicles smaller than 150 nm). Larger ones, belonging to lEVs size category, appear rarely, often with changed morphology, suggesting that their origin was the merging of smaller vesicles (sEVs) after isolation, yet without the confirmation of specific markers it is not possible to exclude the occurrence of native lEVs in the sample. Cryo-TEM images also reveal vesicles at various stages of the merging process. As per the literature, the smallest size of sEVs is considered to be 30 nm, which is consistent with what was observed. There were no EVs visible below 32 nm. To summarise, with the applied isolation protocol it was possible to obtain sEV samples of high purity.

CONCLUSIONS

Hyperglycaemic conditions slightly influenced the mean hydrodynamic radius of EVs. The composition and the structure of an EV corona were not identified. The mode value stayed the same. This suggests that applied conditions may only have an impact on the process of lEVs biogenesis.

Physical sizes measured by Cryo-TEM were consistent and were not changed by the hyperglycaemic conditions. An EV corona was not visible on the acquired images. No impact on morphology was seen either.

The script-based approach to size distribution analysis proved highly precise, offering low standard deviations as well as rapid detection and efficient data management. Manual hand-marking of the EVs did not compromise the quality of the results.

In comparison with NTA, Cryo-TEM is a more precise technique for size distribution analysis, whereas NTA provides a rapid, high--throughput assessment of hydrodynamic radii.

FUNDING

This study was performed with the support of the National Science Centre of Poland through an OPUS 23 grant (Grant ID: 2022/45/B/NZ7/01430), grant holder E. Ł. Stępień. Agnieszka Kyzioł acknowledges the National Science Cente (Poland) within project OPUS 22 (2021/43/B/ST4/02833). The study was carried out using research infrastructure funded by the European Union in the framework of the Smart Growth Operational Programme, Measure 4.2; Grant No. POIR.04.02.00-00-D001/20, ATOMIN 2.0 – Cente for Materials Research on ATOMic Scale for the INnovative Economy.

Research was also partially developed under the provision of the Polish Ministry and Higher Education project Support for Research and Development with the Use of Research Infrastructure of the National Synchrotron Radiation Centre SOLARIS under contract no. 1/SOL/2021/2.

ACKNOWLEDGEMENTS

We thank Kriti Awasthi for her invaluable support in the cell culture and sample preparation. Her expertise and dedication significantly contributed to the success of this work.

DATA AVAILABILITY

Rodbuk UJ (https://uj.rodbuk.pl/): https://doi.org/10.57903/UJ/U2TGUF.

REFERENCES

1. Stępień EŁ, Durak-Kozica M, Moskal P. Extracellular vesicles in vascular pathophysiology: beyond their molecular content. Pol Arch Intern Med. 2023 Apr 19;133(4):16483. https://doi.org/10.20452/pamw.16483.
2. Yáñez-Mó M, Siljander PR, Andreu Z, Zavec AB, Borràs FE, Buzas EI, et al. Biological properties of extracellular vesicles and their physiological functions. J Extracell Vesicles. 2015 May 14;4:27066. doi: https://doi.org/10.3402/jev.v4.27066.
3. Berumen Sánchez G, Bunn KE, Pua HH, Rafat M. Extracellular vesicles: mediators of intercellular communication in tissue injury and disease. Cell Commun Signal. 2021 Oct 16;19(1):104. doi: https://doi.org/10.1186/s12964-021-00787-y.
4. Tucher C, Bode K, Schiller P, Claßen L, Birr C, Souto-Carneiro MM, et al. Extracellular Vesicle Subtypes Released From Activated or Apoptotic T--Lymphocytes Carry a Specific and Stimulus-Dependent Protein Cargo. Front Immunol. 2018 Mar 15;9:534. doi: https://doi.org/10.3389/fimmu.2018.00534.
5. Yang JS, Lee JC, Byeon SK, Rha KH, Moon MH. Size Dependent Lipidomic Analysis of Urinary Exosomes from Patients with Prostate Cancer by Flow Field-Flow Fractionation and Nanoflow Liquid Chromatography-Tandem Mass Spectrometry. Anal Chem. 2017 Feb 21;89(4):2488-2496. doi: https://doi.org/10.1021/acs.analchem.6b04634. Epub 2017 Feb 2. PMID: 28192938.
6. www.who.int [Internet]. "Mean fasting blood glucose". World Health Organization. [cited 2025 Jul 1]. Available from: https://www.who.int/data/gho/indicator-metadata-registry/imr-details/2380#:~:text=The%20expected%20values%20for%20normal%20fasting%20blood%20glucose,changes%20in%2lifestyle%20and%20monitoring%20glycemia%20are%20recommended.
7. Undas A, Podolec P, Zawilska K, Pieculewicz M, Jedliński I, Stepień E, et al. Altered fibrin clot structure/function in patients with cryptogenic ischemic stroke. Stroke. 2009 Apr;40(4):1499–501. https://doi.org/10.1161/STROKEAHA.108.532812.
8. Undas A, Wiek I, Stêpien E, Zmudka K, Tracz W. Hyperglycemia is associated with enhanced thrombin formation, platelet activation, and fibrin clot resistance to lysis in patients with acute coronary syndrome. Diabetes Care. 2008 Aug;31(8):1590–5. doi: https://doi.org/10.2337/dc08-0282.
9. Duncan AE. Hyperglycemia and Perioperative Glucose Management. Curr Pharm Des. 2012;18(38): 6195–203. doi: https://doi.org/10.2174/138161212803832236.
10. Umpierrez GE, Pasquel FJ. Management of Inpatient Hyperglycemia and Diabetes in Older Adults. Diabetes Care. 2017 Apr;40(4):509–17. doi: https://doi.org/10.2337/dc16-0989. PMID: 28325798; PMCID: PMC5864102.
11. Rząca C, Jankowska U, Stępień E. Proteomic profiling of exosomes derived from pancreatic beta-cells cultured under hyperglycemia. Bio--Algorithms and Med-Systems. 2022;18(1):151–7. doi: https://doi.org/10.2478/bioal-2022-0085.
12. Skalska ME, Durak-Kozica M, Stępień EŁ. ToF-SIMS revealing sphingolipids composition in extracellular vesicles and paternal β-cells after persistent hyperglycemia. Talanta. 2025 Jul 15;297(Pt A):128582. doi: https://doi.org/10.1016/j.talanta.2025.128582. Epub ahead of print. PMID: 40684740.
13. www.cnfusers.cornell.edu [Internet]. NANOSIGHT NS300 USER MANUAL, MAN0541-01-EN-00; [cited 2025 Oct 31]. Available from: https://www.cnfusers.cornell.edu/sites/default/files/Equipment-Resources/Nanosight%20NS300%20large%20manual.pdf.
14. refractiveindex.info [Internet]. Open Database: RefractiveIndex.INFO, Refractive index database; [cited 2025 Oct 31]. Available from: https://refractiveindex.info/?shelf=main&book=Au&page=Werner.
15. analytik.co.uk [Internet]. Particle Metrix Particle MetrixGmbH, Introduction to Nanoparticle Tracking Analysis (NTA); [cited 2025 Oct 31]. Available from: https://analytik.co.uk/wpcontent/uploads/2016/12/whitepaper-nanoparticle-tracking-analysis.pdf?utm.
16. Gardiner C, Shaw M, Hole P, Smith J, Tannetta D, Redman CW, et al. Measurement of refractive index by nanoparticle tracking analysis reveals heterogeneity in extracellular vesicles. J Extracell Vesicles. 2014 Nov 24;3:25361. doi: https://doi.org/10.3402/jev.v3.25361. PMID: 25425324; PMCID: PMC4247498.
17. github.com [Internet]. Open Github repository containing written script; [cited 2025 Oct 31]. Available from: https://github.com/maciejslotwinski/Impact-of-Hyperglycemia-on--Cells-EVs-Size-and-Shape.
18. Marzec ME, Rząca C, Moskal P, Stępień EŁ. Study of the influence of hyperglycemia on the abundance of amino acids, fatty acids, and selected lipids in extracellular vesicles using TOF-SIMS. Biochem Biophys Res Commun. 2022 Sep 24;622:30–6. doi: https://doi.org/10.1016/j.bbrc.2022.07.020.
19. Wolf M, Poupardin RW, Ebner-Peking P, Andrade AC, Blöchl C, Obermayer A, et al. A functional corona around extracellular vesicles enhances angiogenesis, skin regeneration and immunomodulation. J Extracell Vesicles. 2022 Apr;11(4):e12207. doi: https://doi.org/10.1002/jev2.12207. PMID: 35398993; PMCID: PMC8994701.
20. Varga Z, Fehér B, Kitka D, Wacha A, Bóta A, Berényi S, et al. Size Measurement of Extracellular Vesicles and Synthetic Liposomes: The Impact of the Hydration Shell and the Protein Corona. Colloids Surf B Biointerfaces. 2020;192:111053. doi: https://doi.org/10.1016/j.colsurfb.2020.111053.
21. van der Pol E, Coumans FA, Grootemaat AE, Gardiner C, Sargent IL, Harrison P, et al. Particle size distribution of exosomes and microvesicles determined by transmission electron microscopy, flow cytometry, nanoparticle tracking analysis, and resistive pulse sensing. J Thromb Haemost. 2014 Jul;12(7):1182–92. doi: https://doi.org/10.1111/jth.12602. Epub 2014 Jun 19. PMID: 24818656.
22. Cavallaro S, Hååg P, Viktorsson K, Krozer A, Fogel K, Lewensohn R, et al. Comparison and optimization of nanoscale extracellular vesicle imaging by scanning electron microscopy for accurate size-based profiling and morphological analysis. Nanoscale Adv. 2021 Mar 22;3(11):3053–63. doi: https://doi.org/10.1039/d0na00948b.
23. Noble JM, Roberts LM, Vidavsky N, Chiou AE, Fischbach C, Paszek MJ, et al. Direct comparison of optical and electron microscopy methods for structural characterization of extracellular vesicles. J Struct Biol. 2020 Apr 1;210(1):107474. https://doi.org/10.1016/j.jsb.2020.107474.
24. Durak-Kozica M, Wróbel A, Platt M, Stępień E. Comparison of qNANO results from the isolation of extracellular microvesicles with the theoretical model. Bio-Algorithms and Med-Systems. 2022;18(1):171–9. doi: https://doi.org/10.2478/bioal-2022-0088.

Supplementary materials are available at Bio-Algorithms and Med-Systems (ISSN: 1896-530X) – online: https://bamsjournal.com/api/myfiles/view/2924517